

Reversible Hydration of $\text{CH}_3\text{NH}_3\text{PbI}_3$ in Films, Single Crystals, and Solar Cells

Aurélien M. A. Leguy,^{†,¶} Yinghong Hu,^{‡,¶} Mariano Campoy-Quiles,[§] M. Isabel Alonso,[§] Oliver J. Weber,[∇] Pooya Azarhoosh,[⊥] Mark van Schilfgaarde,[⊥] Mark T. Weller,[∇] Thomas Bein,[‡] Jenny Nelson,[†] Pablo Docampo,^{*,‡} and Piers R. F. Barnes^{*,†}

[†]Physics Department, Imperial College—London, London, United Kingdom, SW7 2AZ

[‡]Department of Chemistry, Ludwig-Maximilians-Universität, München, Germany, 81377

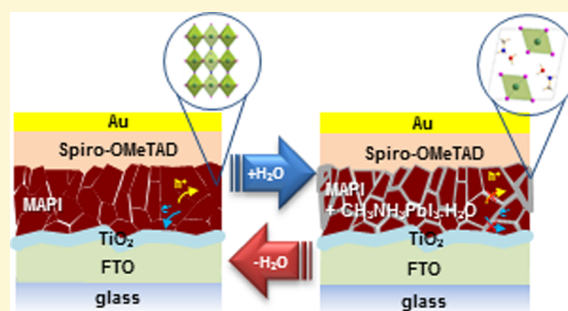
[§]Institut de Ciència de Materials de Barcelona (ICMAB-CSIC), Campus de la UAB, Bellaterra, Spain, 08193

[∇]Centre for Sustainable Chemical Technologies and Department of Chemistry, University of Bath, Bath, United Kingdom, BA2 7AY

[⊥]Physics Department, King's College—London, London, United Kingdom, WC2R 2LS

Supporting Information

ABSTRACT: Solar cells composed of methylammonium lead iodide perovskite (MAPI) are notorious for their sensitivity to moisture. We show that (i) hydrated crystal phases are formed when MAPI is exposed to water vapor at room temperature and (ii) these phase changes are fully reversed when the material is subsequently dried. The reversible formation of $\text{CH}_3\text{NH}_3\text{PbI}_3 \cdot \text{H}_2\text{O}$ followed by $(\text{CH}_3\text{NH}_3)_4\text{PbI}_6 \cdot 2\text{H}_2\text{O}$ (upon long exposure times) was observed using time-resolved XRD and ellipsometry of thin films prepared using “solvent engineering”, single crystals, and state-of-the-art solar cells. In contrast to water vapor, the presence of liquid water results in the irreversible decomposition of MAPI to form PbI_2 . MAPI changes from dark brown to transparent on hydration; the precise optical constants of $\text{CH}_3\text{NH}_3\text{PbI}_3 \cdot \text{H}_2\text{O}$ formed on single crystals were determined, with a bandgap at 3.1 eV. Using the single-crystal optical constants and thin-film ellipsometry measurements, the time-dependent changes to MAPI films exposed to moisture were modeled. The results suggest that the monohydrate phase forms independent of the depth in the film, suggesting rapid transport of water molecules along grain boundaries. Vapor-phase hydration of an unencapsulated solar cell (initially $J_{sc} \approx 19 \text{ mA cm}^{-2}$ and $V_{oc} \approx 1.05 \text{ V}$ at 1 sun) resulted in more than a 90% drop in short-circuit photocurrent and $\sim 200 \text{ mV}$ loss in open-circuit potential; however, these losses were fully reversed after the device was exposed to dry nitrogen for 6 h. Hysteresis in the current–voltage characteristics was significantly increased after this dehydration, which may be related to changes in the defect density and morphology of MAPI following recrystallization from the hydrate. Based on our observations, we suggest that irreversible decomposition of MAPI in the presence of water vapor only occurs significantly once a grain has been fully converted to the monohydrate phase.



INTRODUCTION

Methylammonium lead iodide (which, for simplicity, we will refer to as MAPI) perovskite is generating frenzied interest in the field of alternative photovoltaics as a promising material for achieving the optimum paradigm of the technology: simplicity of processing combined with outstanding optoelectronic properties. The rapid progression of the claimed power conversion efficiencies of MAPI devices—exceeding 20%¹ within five years of the first publication²—raises the hope that the technology will lead to the manufacture of highly efficient photovoltaic modules with a short energy payback time, relative to established technologies.³

Ensuring the stability of MAPI photovoltaics under operational conditions is one of the biggest barriers to commercializing the technology. At present, little is understood about the failure mechanisms of devices. To develop effective strategies to

improve stability and achieve market standards, the degradation pathways under different environmental conditions must be elucidated.

Unmistakably, MAPI is sensitive to moisture, which may have both detrimental and beneficial effects, depending on the context. The presence of humidity during film processing has been shown to significantly influence thin film morphology⁴ and was claimed to lead to an improvement of the performance of solar cells.^{5,6} However, the presence of water has also been suggested (e.g., by Frost et al.⁷) to catalyze the irreversible decomposition of MAPI into aqueous HI, solid PbI_2 , and CH_3NH_2 either released as gas or dissolved in water.

Received: February 19, 2015

Revised: April 2, 2015

Published: April 5, 2015

Experimental evidence has been published to confirm the degradation of MAPI into PbI_2 ⁸ while, in parallel, water was suggested to provoke the crystallization of a perovskite species incorporating isolated $[\text{PbI}_6]^{4-}$ octahedra.⁹ It has been shown that the exposure of MAPI solar cells to a relative humidity greater than ~50% has rapid detrimental consequences on device performances.¹⁰ Thus, efforts to prevent moisture ingress¹¹ or careful device encapsulation are required to achieve significant stability under operation.¹²

This paper concerns the interaction of MAPI with water. The formation of colorless monohydrated methylammonium lead iodide ($\text{CH}_3\text{NH}_3\text{PbI}_3\cdot\text{H}_2\text{O}$) from MAPI crystals in aqueous solution at temperatures below 40 °C was described in 1987 by Poglitsch and Weber.¹³ The structure of this monohydrate was later determined by Hao et al.¹⁴ The compound (CH_3NH_3)₄ $\text{PbI}_6\cdot 2\text{H}_2\text{O}$, which we will occasionally refer to as dihydrated methylammonium lead iodide, can also be formed by a similar method, as described by Vincent et al.¹⁵ Pale yellow dihydrate crystals result when MAPI is cooled to below 40 °C in a mother liquor of aqueous $\text{Pb}(\text{NO}_3)_2$ and methylammonium iodide solution. Christians and co-workers recently investigated the interaction of MAPI and water vapor by exposing both MAPI films cast on mesoporous Al_2O_3 and full solar cells to controlled humidity,¹⁶ while, concurrently, Yang et al. have investigated the influence of different hole transport materials on devices exposed to moisture.¹⁷ Both identified the degradation product as (CH_3NH_3)₄ $\text{PbI}_6\cdot 2\text{H}_2\text{O}$; we note that their diffraction patterns suggest a significant contribution from the monohydrate species. In addition, Christians et al. observed a decrease in performance of solar cells that were stored in moist air, depending on the level of humidity. Zhao et al.¹⁸ reported instant optical bleaching of MAPI thin films upon exposure to ammonia vapor that was fully reversible. Their observation was characterized by the appearance of a new Bragg reflection (Cu $K\alpha$ radiation) at $\sim 11.6^\circ 2\theta$ in the XRD pattern of the bleached MAPI species. Although not yet widely appreciated, MAPI clearly shows a propensity to form new solvated crystal structures at room temperature by incorporating small polar molecules. To the best of our knowledge, the full reversibility of the stepwise hydration of MAPI has not yet been demonstrated.

Here, we combine time-resolved ellipsometry with X-ray diffraction (XRD) measurements to identify the degradation products and monitor the dynamics of the decomposition reactions on thin films, single crystals, and full devices in the presence of moisture. Besides the precise derivation of the optical constants of both MAPI single crystals and the hydrate species, our results elucidate the hydration mechanisms and differentiate between reversible hydration and the irreversible formation of lead iodide, thus constituting a crucial step toward engineering long-term stability in perovskite solar cells. Finally, we show that devices that have been exposed to moisture exhibit a dramatic loss of performance, which may be recovered by a simple drying step at room temperature, as long as water condensation on the perovskite surface did not occur.

METHODS

Sample Preparation. MAPI Single Crystals. Methylammonium lead iodide (MAPI) single crystals were grown according to the method of Poglitsch and Weber.¹³ 2.5 g of lead acetate trihydrate ($\text{Pb}(\text{CH}_3\text{CO}_2)_2\cdot 3\text{H}_2\text{O}$, Sigma) was dissolved in 10 mL of hydroiodic acid (HI_{aq} , 57 wt %, Sigma) in a 50 mL round-bottom flask and heated to 100 °C in an oil bath. Separately, 0.597 g of CH_3NH_2 (aq, 40%,

Sigma) was added dropwise to an additional 2 mL of HI_{aq} kept at 0 °C in an ice bath under stirring. The methylammonium iodide solution was then added to the lead acetate solution and the mixture was cooled over 5 days to a temperature of 46 °C, resulting in the formation of black crystals with the largest face length being ~ 8 mm. The content of the flasks was subsequently filtered and dried for 12 h at 100 °C.

MAPI Hydrate Single Crystals. The formation of a hydrated form of MAPI perovskite single crystals below 40 °C was first mentioned by Weber.¹⁹ In a 250 mL round-bottom flask, 12 mL of CH_3NH_2 (40 wt % in H_2O , Sigma) was neutralized by an aqueous solution of concentrated HI solution (57 wt % in H_2O) until the indicator paper showed a value of pH 7, and the mixture was heated to 100 °C. Subsequently, 3.86 g of $\text{Pb}(\text{NO}_3)_2$ dissolved in 18 mL of H_2O was added dropwise to the hot MAI solution under vigorous stirring and black MAPI crystallites started to precipitate. Slowly cooling the solution down to room temperature (over 4 h) led to the transformation of the black crystallites to thin, pale yellow needles. After exposing the crystals to the mother liquor overnight in a refrigerator, the pale yellow needles were filtrated, washed with 50 mL of dichloromethane, and dried under vacuum (50 mbar) for 1 h. The product obtained was metastable and turned into grayish polycrystalline MAPI by the spontaneous loss of its crystalline water under ambient conditions. To avoid this, the sample was stored in a jar at 77% RH in order to prevent dehydration in air ($\sim 35\%$ RH).

MAI Crystals. $\text{CH}_3\text{NH}_3\text{I}$ (MAI) single crystals were synthesized by reacting 24 mL CH_3NH_2 (33 wt % in absolute ethanol, Sigma) diluted in 100 mL of absolute ethanol and 10 mL of HI (57 wt % in H_2O , Sigma) at 0 °C in a 250 mL round-bottom flask for 2 h under stirring at room temperature, respectively. After removal of the solvent with a rotary evaporator at 50 °C, the white precipitate was recrystallized from absolute ethanol, washed with diethyl ether, and dried under vacuum for 12 h.

Thin Film Preparation. Perovskite thin film preparation was conducted in a glovebox under a dry nitrogen atmosphere. Thin films of MAPI were fabricated following a “solvent engineering” procedure reported by Xiao et al.²⁰ First, glass substrates with dimensions of 2.5 cm \times 2.5 cm were cleaned with deionized (DI) water, absolute ethanol, dried under air flow, and then treated in a plasma cleaner with an oxygen plasma for 5 min. For an equimolar 1.25 M MAPI perovskite precursor solution, 0.4 g of MAI and 1.156 g of PbI_2 (99%, Aldrich) were dissolved in 2 mL of dimethylformamide (DMF) (anhydrous, 99.8%, Aldrich) under stirring at 100 °C. Subsequently, 50 μL of the solution was dynamically spin-coated on a clean glass substrate at 6000 rpm. After a delay of 4 s, 150 μL of chlorobenzene (anhydrous, 99.8%, Aldrich) was quickly added to the spinning substrate. After a total spinning time of 30 s, the substrate was immediately annealed at 100 °C for 10 min to evaporate residual solvents and to further promote crystallization. Dark brown, lustrous films of MAPI were obtained with a thickness of ~ 270 nm, as determined with a Veeco DekTak profilometer.

Solar Cell Fabrication. Fluorine-doped tin oxide (FTO)-coated glass substrates (Pilkington, 7 Ω/sq) were cut into pieces 3 cm \times 3 cm in size and patterned by etching with Zn metal powder and 3 M HCl diluted in DI water. The substrate were then cleaned with an aqueous 2% Hellmanex detergent solution, rinsed with DI water, acetone, and ethanol, and finally dried under an air flow. The patterned substrates were cleaned with oxygen plasma for 5 min. A TiO_2 compact layer was deposited on top of the substrates, using a sol-gel process. For this purpose, a solution containing 35 μL of 2 M HCl and 2.5 mL of dry 2-propanol (IPA) was added dropwise to a solution of 369 μL of titanium isopropoxide ($\geq 97\%$, Sigma) in 2.5 mL of dry IPA under strong stirring. The substrates were coated with the TiO_x sol-gel solution by spin-coating dynamically at 2000 rpm for 45 s and then quickly placed on a hot plate at 150 °C for 10 min. To complete the transformation of TiO_x into the anatase phase, the coated substrates were gradually heated to 500 °C (using a ramp of 8 °C/min) and sintered for 45 min in air. A 280 nm MAPI perovskite thin film was deposited on top of the TiO_2 compact layer by following the same

“solvent engineering” process as employed for thin films, but with a slightly slower spinning rate during spin-coating (5000 rpm).

In order to add the hole transporter to the devices, a solution of 2,2',7,7'-tetrakis(*N,N*-di-*p*-methoxyphenyl-amine)-9,9'-spirobifluorene (spiro-OMeTAD, 99.56%, Borun Chemicals) in anhydrous chlorobenzene (100 mg/mL) was filtered with a 0.45 μm syringe filter and mixed with 10 μL of 4-*tert*-butylpyridine (96%, Aldrich) and 30 μL of a 170 mg/mL solution of lithium bis-trifluoromethanesulfonimide (Li-TFSI, 99.95%, Aldrich) in acetonitrile (anhydrous, 99.8%, Aldrich) per 1 mL spiro-OMeTAD solution. The hole transporter solution was coated onto the device substrate by a consecutive two-step spin-coating process at 1500 and 2000 rpm for 40 and 5 s, respectively. Afterward, the substrates were removed from the glovebox and stored overnight in a desiccator at $\sim 35\%$ RH. Finally, a 40 nm thick gold layer was deposited by thermal evaporation through a patterned shadow mask under high vacuum conditions (4×10^{-6} mbar) to form the counter electrode. The active area under the mask was 0.083 ± 0.002 cm².

Ellipsometry Measurement. Spectrometric ellipsometry data on thin films were gathered using an ellipsometer (Model ESM-300, J. A. Woollam Co., Inc.). Measurements on single crystals were performed with a SOPRALAB GESSE rotating polarizer ellipsometer mounted in a vertical configuration, which is better suited for single crystals. Optical spectra on single crystals were recorded from ca. 1.2 eV to 5.5 eV, at three incidence angles for each sample (67.5°, 70°, and 75°). *In situ* measurements during hydration and dehydration were performed at fixed incidence (67.5° for single crystals and 75° for thin films). For the single-crystal measurements, the ellipsometer was equipped with a chamber fitted with two small slits to offer the possibility to measure the samples at different angles of incidence. In the case of thin films, the measurement was taken through quartz windows, the gas flow being introduced through a side opening. The acquisition time of a spectrum was sufficiently short (less than 5 s), compared to the time scale of the measurement to be considered as instantaneous in the analysis.

The Hydration Setup for Ellipsometry Measurements. For single-crystal ellipsometry, the relative humidity was fixed at 70% ($\pm 5\%$) by controlling the ratio of a mixture of dry nitrogen to humid nitrogen that traveled through a bubbler at room temperature (21 °C). The gas mixture was used to fill the measurement chamber, which had a positive pressure difference relative to the laboratory atmosphere. A similar setup was employed for the analysis of *in situ* hydration of thin films and full solar cell devices, but compressed filtered air as carrier gas with relative humidity of 80% ($\pm 5\%$) was used in place of nitrogen. The relative humidity was controlled with a calibrated hygrometer.

Ellipsometry Fitting. Spectrometric data acquired by means of varying angle spectroscopic ellipsometry was analyzed using the WVASE 32 software (J. A. Woollam Co., Inc.) for thin films and Winelli2 software (SOPRALAB) for single crystals. To fit the experimental data, an initial model of the optical transitions was built for each layer constituting the sample. The dielectric constant was described as a sum of the critical points (CPs) of the joint density of states:

$$\epsilon(E) = UV_{\text{term}} - \sum_{i=1}^N [A_i e^{j\phi_i} (E - E_{ci} + j\Gamma_i)^{n_i}] \quad (1)$$

where N is the number of CPs in the model, E is the incident photon energy, j is the imaginary unit, and UV_{term} is a constant accounting for high-energy transitions. Critical point i is described by an amplitude A_i , energy E_{ci} , line width Γ_i , exciton phase angle ϕ_i , and dimensionality n_i .²¹ The dielectric function is then calculated from the model, which enables the software to simulate spectrometric values of the ellipsometry parameters, ψ and Δ , at the angles of incidence used for the acquisition via transfer matrix calculations. The ellipsometry parameters relate to the Fresnel coefficients R_p and R_s for p- and s-polarized light:

$$\frac{R_p}{R_s} = \tan(\psi) e^{i\Delta} \quad (2)$$

Finally, a regression algorithm was used to fit the modeled curve to the experimental ψ and Δ data by varying the free parameters (for example: the layer thickness and the amplitude or energy center of an oscillator). The figure of merit describing quantitatively the quality of the fits is the mean square error (MSE), given by

$$\text{MSE} = \sqrt{\frac{1}{2N' - M} \sum_{i=1}^{N'} \left[\left(\frac{\psi_i^{\text{mod}} - \psi_i^{\text{exp}}}{\sigma_{\psi,i}^{\text{exp}}} \right)^2 + \left(\frac{\Delta_i^{\text{mod}} - \Delta_i^{\text{exp}}}{\sigma_{\Delta,i}^{\text{exp}}} \right)^2 \right]} \quad (3)$$

where N' is the number of (ψ, Δ) pairs, M the number of variable parameters in the model (“mod”), and σ describes the standard deviations on the experimental (“exp”) data points.

The Bruggeman Approximation. The Bruggeman approximation is an analytical averaging method commonly used to study the macroscopic properties of composite materials. In the case of ellipsometry modeling, the approximation is used to estimate the optical constants of two (or more) intimately mixed phases. It assumes homogeneous dispersion of one phase into another, resulting in an effective medium (EMA). The effective dielectric function $\tilde{\epsilon}$ of a material composed of two constituents A and B (with respective volume fractions f_A and f_B) can thus be written as

$$f_A \left(\frac{\tilde{\epsilon}_A - \tilde{\epsilon}}{\tilde{\epsilon}_A - 2\tilde{\epsilon}} \right) = -f_B \left(\frac{\tilde{\epsilon}_B - \tilde{\epsilon}}{\tilde{\epsilon}_B - 2\tilde{\epsilon}} \right) \quad (4)$$

This complex equation, which is also called the coherent potential approximation, is solved numerically for $\tilde{\epsilon}$. The surface roughness between two layers is also commonly described by an EMA layer consisting of a composite of top and bottom material in equal proportion. In the particular case of top-layer roughness, an EMA is used with identical volume proportion of both the top layer and voids.²²

X-ray Diffraction Measurements. XRD measurements on both thin films and powder samples were performed using a Bruker D8 Discover X-ray diffractometer operating at 40 kV and 30 mA, employing Ni-filtered Cu $K\alpha$ radiation ($\lambda = 1.5406$ Å) and a position-sensitive detector (LynxEye). During the XRD measurements, the samples were exposed to ambient conditions (21 °C, 35%–40% RH). In order to minimize the influence of the environmental factors on the samples during the measurements, the XRD patterns were acquired by recording at a standard 2θ step size of 0.05° and a scan speed of 40 deg s⁻¹.

Measurements on Solar Cells. The J - V characteristics of planar perovskite solar cell devices were measured using a Newport Model OriSol 2A solar simulator with a Keithley Model 2401 source meter. The devices were illuminated through a shadow mask, yielding an active area of 0.0813 ± 0.002 cm². The J - V curves were recorded under standard AM 1.5G illumination, calibrated to a light intensity of 100 mW cm⁻² with a silicon cell (Fraunhofer ISE certified). The input bias voltage was scanned from reverse (-2 V) to forward (0 V) (referred to as backward scan) in 0.05 V steps with a rate of 0.5 V s⁻¹ and then from forward to reverse bias (0 to -2 V, forward scan) at the same rate.

RESULTS AND DISCUSSION

Single Crystals. The hydration mechanism was first investigated optically by varying angle spectroscopic ellipsometry on single crystals of MAPbI₃. The single crystals were prepared via the method of Poglitsch and Weber¹³ recapitulated in the Methods section. Figure 1 shows the optical characterization and reversibility upon hydration of what was initially a single crystal of MAPbI₃. When exposed to 70% relative humidity (RH) at room temperature, the bandgap of the crystal underwent a change from ~ 1.6 eV to 3.1 eV within ~ 60 h. The final product is a hydrate constituting a new phase that does not show any of the features of the pristine material. It will be

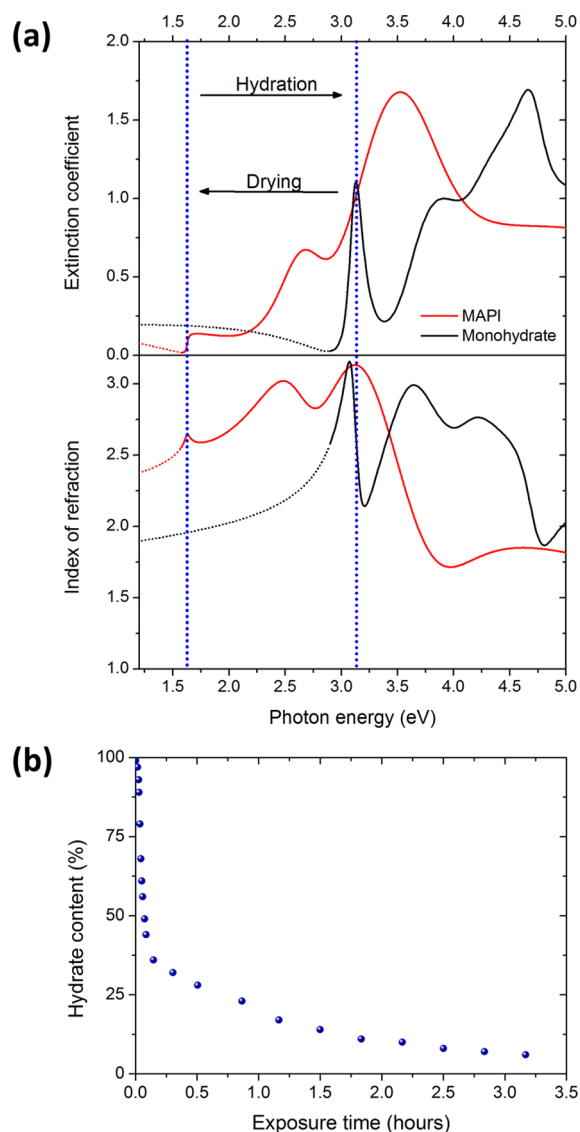


Figure 1. (a) Optical constants of MAPI (solid red line) and the hydration product (solid black line) modeled from single crystal ellipsometry (see Tables S5 and S6 in the Supporting Information). The dotted part of the spectra corresponds to the sub-bandgap region. The vertical dotted blue lines help to visualize the shift of the bandgap energy upon hydration and drying. (b) Fraction of $\text{CH}_3\text{NH}_3\text{PbI}_3 \cdot \text{H}_2\text{O}$ that has not been converted back to MAPI as a function of drying time. The measurement was performed on a single crystal of MAPI that had previously been hydrated by exposure to moisture (70% RH, room temperature) for 60 h until no MAPI was detectable by ellipsometry.

shown below that this hydrate, which has been observed to form at the early stages of the hydration of MAPI crystals, is the monohydrate phase. When subsequently exposed to a dry atmosphere, the hydrate instantly starts to convert back to the initial MAPI perovskite structure, with the process ending in the full recovery of the material (see Figure S1 in the Supporting Information) within ~ 4 h. The layer thickness probed by ellipsometry can be estimated crudely from the optical penetration depth δ_p (where $\delta_p = \lambda_0 / (4\pi\kappa)$, with λ_0 being the incident wavelength and κ being the extinction coefficient). The probed depth thus varies between ~ 300 nm for 1.6 eV photons to only ~ 30 nm at 3.1 eV. Since the hydrate spectrum presents no feature at ~ 1.6 eV, we conclude that full

conversion from MAPI to the hydrate occurred to at least the penetration depth within the crystal, such that only one species was being examined in each measurement.

The dielectric functions of both MAPI and the monohydrate phase were modeled by fitting an ensemble of critical points of the joint density of states to the measured ellipsometry parameters according to the approach described in the Methods section. The fits of the ellipsometry parameters of the hydrate are given in Figure S2 in the Supporting Information; we believe that this is the first optical characterization of this material. The precise derivation of the optical properties of MAPI single crystals will be published separately and is consistent with the recent optical characterization of MAPI thin films in refs 23–25. (The optical constants are given in tabulated form in Table S5 in the Supporting Information.) We note that literature values of the MAPI bandgap range from 1.5 eV to 1.6 eV, the spread in this quantity appears to be due to differences in the measurement techniques and the definition of the band gap^{23–27} and recent observations suggest that aging effects may also increase the band gap.²⁸ For the purposes of this study, we will use the energy of the first critical point required to fit the ellipsometry data, which are also consistent with the energy of the photoluminescence peak. We note that this quantity is not identical to the bandgap determined from a Tauc plot of powder reflectance, which requires a more accurate determination of the absorption tail; this is a feature that is not well-characterized by ellipsometry. Excitonic critical points (0D, $n = -1$ in eq 1) were suitable for describing the optical transitions. In particular, the bandgap transition was found to be strongly excitonic (see Figure S3 and Table S1 in the Supporting Information) with a symmetric Lorentzian line shape, because of a high degree of localization of the exciton on the octahedra, as explained below.

Surface roughness was modeled by an effective medium approximation layer, as explained in the Methods section. The best fits gave values of the surface irregularity around 20 nm for MAPI single crystals and 15 nm in its hydrated form (note that these values should be considered as fitting parameters accounting for the imperfection of the crystal surface rather than representing the absolute root-mean-square (rms) roughness). Some uncertainty remains regarding the optical constants in the sub-bandgap region (dotted lines in Figure 1), as the calculated values can be influenced by the tail of the critical points.

A comparison between the position of the CPs of MAPI and its hydrated counterpart is given in Table 1. The position of the fifth CP of the hydrate is ambiguous, since it is located outside the probed spectral region. It accounts for transitions occurring

Table 1. Critical Point Energies Obtained for the Best Fit of MAPI and Its Hydrate^a

critical point, CP	CP position in MAPI (eV)	CP position in the hydrate (eV)
1	1.6	3.1
2	2.6	3.6
3	3.1	4.2
4	3.6	4.7
5	4.8	10.9

^aThe complete model of the hydrate is given in Table S2 in the Supporting Information.

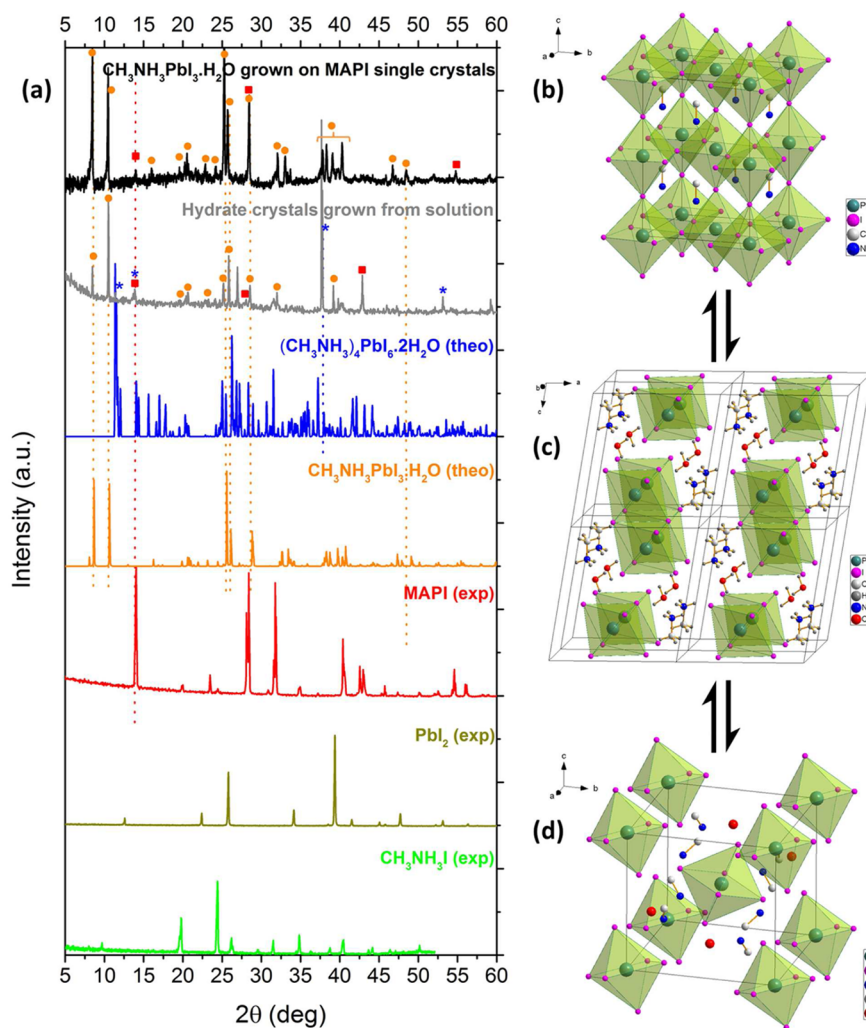


Figure 2. (a) Identification of the composition of the hydrate species grown on MAPI single crystals (at long exposure to water vapors) and of MAPI hydrate crystals (polycrystalline, obtained from solution) by X-ray diffraction (XRD) (patterns in black and gray). The five patterns below these (either experimentally measured or simulated from crystal structures) show species the hydrated crystal material is likely to contain. Symbols are used to tag the main features according to the color of their respective spectra. Panel (b) shows the structure of MAPI in its cubic phase, while panel (c) shows the structure of the monohydrate phase, $\text{CH}_3\text{NH}_3\text{PbI}_3 \cdot \text{H}_2\text{O}$ and (d) displays the structure of the dihydrate, $(\text{CH}_3\text{NH}_3)_4\text{PbI}_6 \cdot 2\text{H}_2\text{O}$. The position of the hydrogens on the $(\text{CH}_3\text{NH}_3)^+$ ions and the water is not assigned in panels (b) and (d).

at higher energies which could not be accurately characterized with the apparatus employed in this study.

We now analyze the structure of hydrated MAPI. XRD patterns were collected from MAPI single crystals that were exposed to water vapor (80% RH during 60 h; see the Methods section).

The XRD pattern in Figure 2a indicates that the MAPI single crystal has converted to a monohydrate, $\text{CH}_3\text{NH}_3\text{PbI}_3 \cdot \text{H}_2\text{O}$. The simulated XRD pattern for each phase^{14,15} (also shown in Figure 2a) enable clear identification of the strong reflections at $2\theta = 8.47^\circ$ and $2\theta = 10.54^\circ$ as MAPI monohydrate.

The monohydrate, $\text{CH}_3\text{NH}_3\text{PbI}_3 \cdot \text{H}_2\text{O}$, was reported to form metastable, thin, pale yellow needles (see Figure S4 in the Supporting Information) that dehydrate spontaneously in air, forming polycrystalline MAPI.¹⁴ Figure 2c shows the refined crystal structure of this intercalation compound.¹⁴ It incorporates one-dimensional (1D), isolated $[\text{PbI}_3]^-$ double-chains, in which each $[\text{PbI}_6]^{4-}$ octahedron is connected to two neighboring octahedra by a common corner, forming a two-octahedra-wide “ribbon” (extending out of the page, along the b -axis in Figure 2c). These negatively charged $[\text{PbI}_3]^-$ chains

are charge-balanced by the intercalated CH_3NH_3^+ cations. In addition, the H_2O molecules that are inserted between the $[\text{PbI}_3]^-$ chains provide further stability to the structure via symmetrically bifurcated hydrogen bonds between the H atoms of the water molecules and the N atom of methylammonium cations ($d_{\text{O-N}} = 2.829 \text{ \AA}$).¹⁴ The calculated XRD pattern of $\text{CH}_3\text{NH}_3\text{PbI}_3 \cdot \text{H}_2\text{O}$ exhibits intense Bragg peaks at the 2θ positions 8.10° , 8.66° , and 10.66° , corresponding to the (001), (100), and $(\bar{1}01)$ reflections of a monoclinic $P2_1/m$ crystal structure. In the XRD pattern of the MAPI film exposed to moisture in Figure 2a, the presence of monohydrate can be recognized by reflections at $\sim 8.6^\circ$ and 10.5° .

The monohydrate, $\text{CH}_3\text{NH}_3\text{PbI}_3 \cdot \text{H}_2\text{O}$, should not be confused with the related dihydrate crystal structure, $(\text{CH}_3\text{NH}_3)_4\text{PbI}_6 \cdot 2\text{H}_2\text{O}$. Dihydrate crystals are obtained—together with the monohydrate species—in directly synthesized hydrated MAPI needle-shaped crystals prepared from solution (see the Methods section, photographs in Figure S4 in the Supporting Information, with a characteristic reflection at $2\theta = 11.39^\circ$ in the XRD patterns in Figure 2a). The dihydrate, $(\text{CH}_3\text{NH}_3)_4\text{PbI}_6 \cdot 2\text{H}_2\text{O}$, can be considered as a zero-dimen-

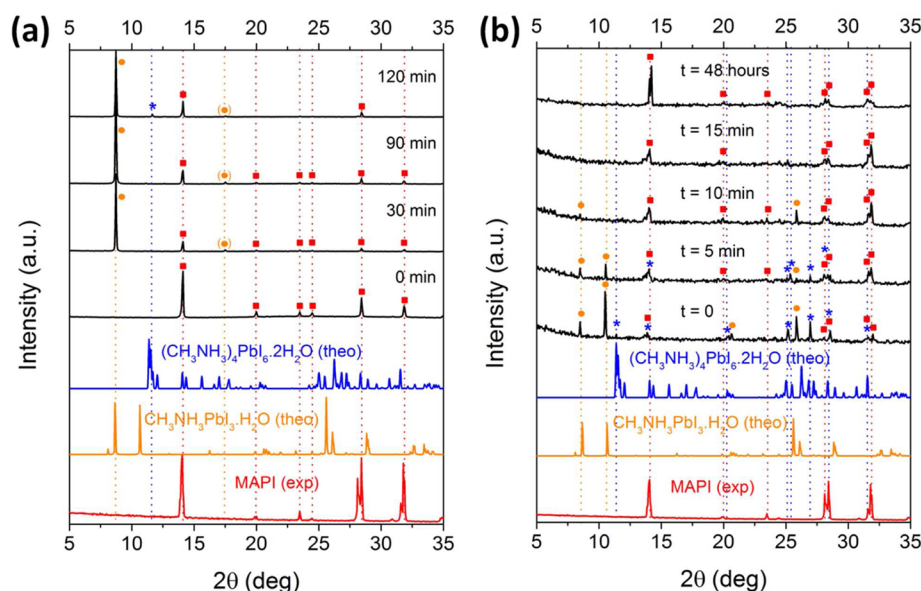


Figure 3. Time-resolved XRD patterns of polycrystalline MAPI: (a) hydration of a MAPI thin film and (b) dehydration of directly synthesized hydrate needlelike crystals.

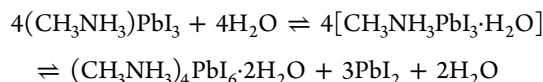
sional network of isolated $[\text{PbI}_6]^{4-}$ octahedra, neutralized by surrounding CH_3NH_3^+ cations. The crystal structure can be related to a distorted NaCl-type lattice consisting of $[\text{PbI}_6]^{4-}$ octahedra and $(\text{CH}_3\text{NH}_3 \cdots \text{H}_2\text{O} \cdots \text{CH}_3\text{NH}_3)_2^{4+}$ dimers (see Figure 2d).¹⁵ The simulated XRD pattern in Figure 2a shows that this compound has a diffraction peak at $\sim 11.4^\circ$. Papavassiliou et al. reported the value of 3.87 eV for the position of the bandgap of $(\text{CH}_3\text{NH}_3)_4\text{PbI}_6 \cdot 2\text{H}_2\text{O}$ by optical absorption spectroscopy.²⁹ The absence of any feature in the absorption spectrum obtained from the ellipsometry results in Figure 1 combined with the clear assignment of the XRD peaks to $\text{CH}_3\text{NH}_3\text{PbI}_3 \cdot \text{H}_2\text{O}$ in Figure 2a rules out the presence of any significant amount of dihydrate in the hydrated MAPI single crystals.

Thin Films and Polycrystals. The study was next extended to thin films. MAPI films were prepared on glass using the “solvent engineering” approach described in the Methods section and then exposed to air with a RH of $\sim 80\%$ for 2 h. XRD patterns displayed in Figure 3a show that the exposure to moist air resulted in the conversion of MAPI to both the monohydrate and dihydrate species.

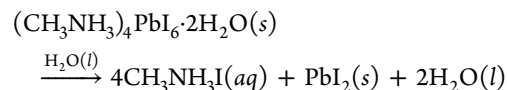
Although both hydrate species coexist in the MAPI film after prolonged exposure to moisture, their formation is not simultaneous. Time-resolved XRD experiments were performed to monitor the dynamics of the hydration and dehydration processes in MAPI and to identify the composition of the samples at different transformation stages. The MAPI films were exposed to an airflow containing $80\% \pm 5\%$ RH. For exposure times of 30 and 60 min, the XRD patterns exhibit a very strong reflection at 8.72° , in addition to the characteristic reflections of pristine MAPI, indicating the formation of $\text{CH}_3\text{NH}_3\text{PbI}_3 \cdot \text{H}_2\text{O}$ (see Figure 3a). After 120 min, an additional reflection at 11.64° was detected, indicating the formation of crystalline $(\text{CH}_3\text{NH}_3)_4\text{PbI}_6 \cdot 2\text{H}_2\text{O}$ in the perovskite film. We conclude that the hydration reaction of MAPI is a two-step process, in which the crystal structure of MAPI is first progressively saturated with one water molecule per formula unit, followed by the formation of a new structure with two water molecules per formula unit upon longer exposure to

humidity. The intercalation of water molecules into the crystal structure of MAPI induces a rearrangement resulting in the separation of the $[\text{PbI}_6]^{4-}$ octahedra, corresponding to the transition from a three-dimensional (3D) network of octahedra in pristine MAPI, to one-dimensional (1D) double-chains in the monohydrated MAPI species, and finally resulting in a zero-dimensional (0D) framework of isolated octahedra in MAPI dihydrate. This crystallographic observation substantiates the idea of a high degree of localization of the exciton in the MAPI hydrate, which is suggested by our ellipsometry measurements.³⁰

The composition of the hydrate species and their sequential formation suggests the following stoichiometric equation:



The monohydrate is an intermediate product that can be easily converted back to MAPI.¹⁴ When the reaction is driven further to the right by prolonged exposure to water vapor, the formation of the dihydrate is initiated, accompanied by the formation of lead iodide (PbI_2) and the release of two water molecules. Only traces of PbI_2 were detected in the XRD patterns. The reason may be that the PbI_2 formed is initially in an amorphous or nanocrystalline phase, presumably pushed out of the hydrate crystals to grain boundaries. The release of water as the reaction goes from the monohydrate to the dihydrate suggests partial self-sustainability of the conversion process as the water molecules released can be reused to convert remaining MAPI into the monohydrate. It seems likely that the reversibility of monohydrate-to-dihydrate conversion may be limited by phase separation of the reaction products. Eventually, when the entire film is converted, an excess of water may result in the dissolution of CH_3NH_3^+ , irreversibly degrading the structure:



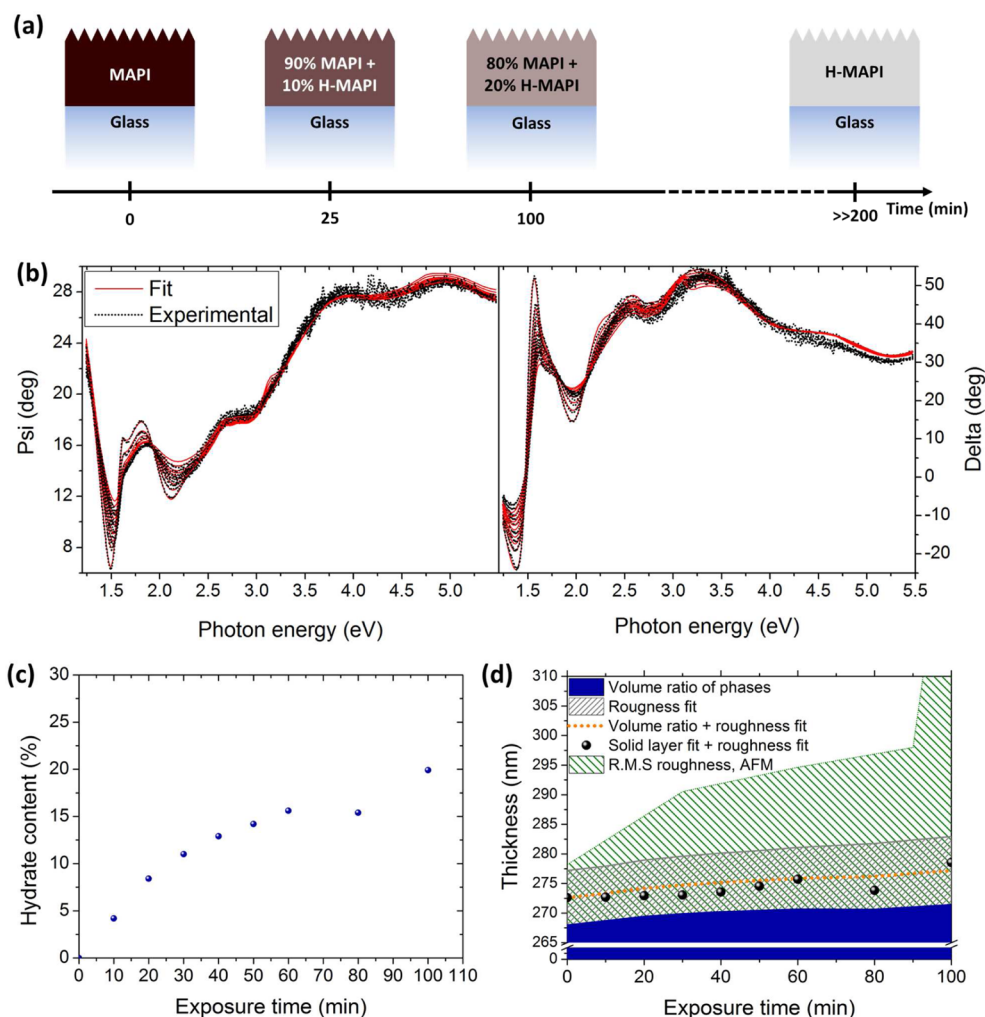


Figure 4. (a) The Bruggeman-type degradation mechanism used to model the ellipsometry parameters. (b) Representative fits of the ellipsometry parameters obtained using the Bruggeman model at different thickness exposure times. (c) Hydrate proportion in the thin film as a function of exposure time to humid air (80% RH). (d) Cumulative plot of the thickness increase, which is due to the conversion from MAPI to hydrate species. The blue area shows the solid layer thickness inferred from the relative ratio of phases determined from the fit of the ellipsometry models (see panel (c)). The hatched gray area is the surface roughness inferred from the fit of the ellipsometry model assuming 50% of voids and 50% of solid layer (blue) in the rough region. The orange dotted line gives the total equivalent layer thickness defined by the blue area plus half of the gray. It can be compared with the black dots showing the total equivalent layer thickness obtained from the fit of the ellipsometry model, assuming solid layer (blue) and half of gray. The hatched green area gives the rms roughness measured by AFM.

The exposure of $(\text{CH}_3\text{NH}_3)_4\text{PbI}_6 \cdot 2\text{H}_2\text{O}$ to light may also result in its irreversible decomposition without the requirement for excess water.^{11,16}

The reverse dehydration reactions were observed to spontaneously occur when hydrated MAPI crystals were exposed to air with low humidity (35% RH at 21 °C). In order to track the dehydration reactions, XRD patterns were recorded in 5 min intervals, shown in Figure 3b. During the exposure to “dry” air, the crystals changed color from yellow to dark gray, indicating the formation of polycrystalline MAPI as water molecules were lost.

Figure 3b shows that after only a few minutes of drying, characteristic XRD reflections of pristine MAPI appeared in the diffraction patterns. Longer drying times led to the disappearance of the reflection at 11.39° , corresponding to complete transformation of crystalline MAPI dihydrate to other phases. The reduction of this reflection intensity is accompanied by a decrease of the reflection intensities associated with MAPI monohydrates and a concomitant increase in the intensity of

the crystalline MAPI reflections. This gradual transformation of hydrated MAPI into MAPI perovskite crystals ends in the formation of MAPI within ~ 15 min, as demonstrated by the XRD patterns showing only the reflections of tetragonal MAPI. We observed that, for crystallites of similar sizes, dehydration appears to be a faster process than hydration at room temperature.

Although crystallites of hydrated MAPI were previously reported to have a pale yellow color,^{14,15} our optical characterization, which we assign to the monohydrate phase, indicated that the material is almost colorless. This observation is corroborated by reflectometry measurements performed by Hirasawa et al. in the 1990s.³¹ The pale yellow color of macroscopic MAPI hydrate needles reported previously may originate from defects, disorder, or impurities (for example, traces of elemental iodine, which can evolve in the mother liquor from oxidation of concentrated HI solutions, or from the formation of PbI_2 when $\text{CH}_3\text{NH}_3\text{PbI}_3 \cdot \text{H}_2\text{O}$ converts to $(\text{CH}_3\text{NH}_3)_4\text{PbI}_6 \cdot 2\text{H}_2\text{O}$).

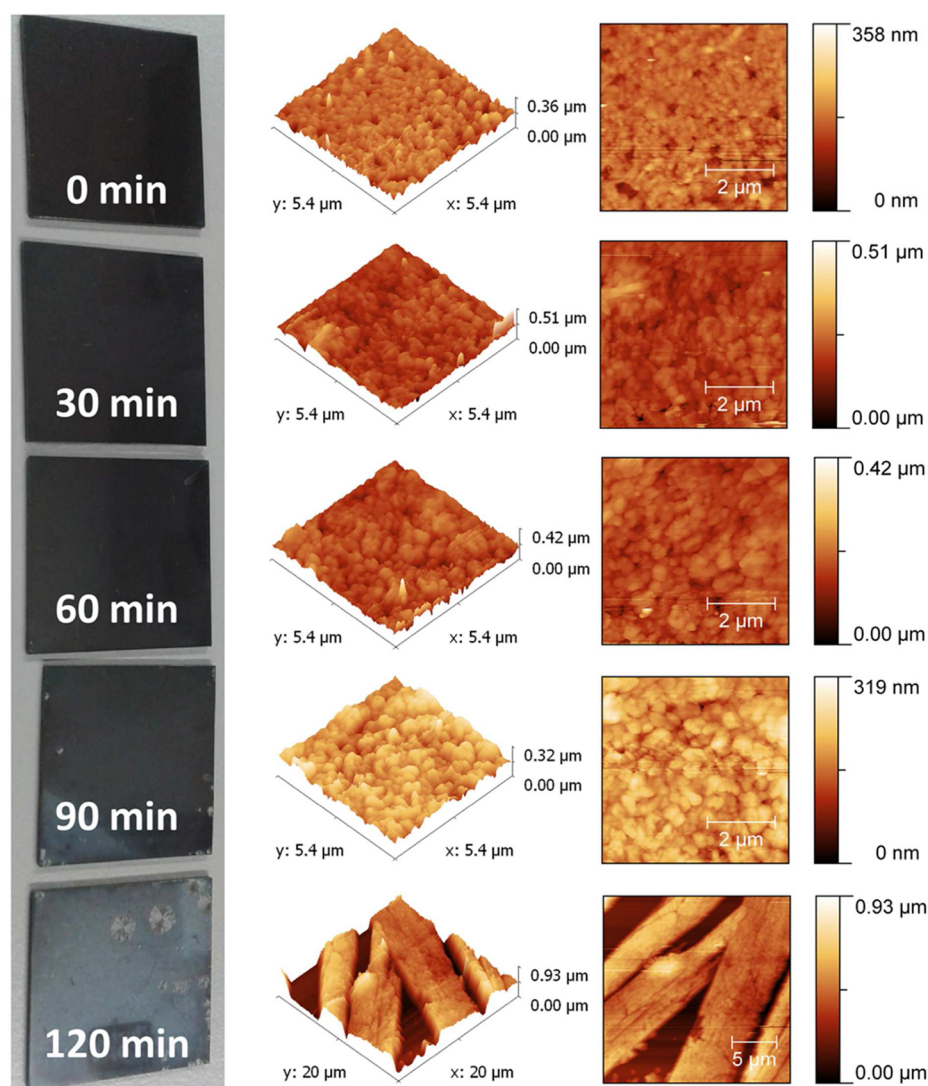


Figure 5. Photographs of thin films of MAPI deposited on glass at different hydration times showing discoloration and AFM measurements (3D and 2D representations).

We reiterate that the MAPI film hydration process did not initially lead to the formation of a substantial amount of crystalline PbI_2 . We speculate that the mechanism of irreversible decomposition of MAPI into HI, PbI_2 , and CH_3NH_2 can only happen in the presence of excess or liquid water which can dissolve the methylammonium ions. We substantiated this hypothesis by exposing a thin film of MAPI to warm water vapors (see Figure S5 in the Supporting Information). Water condensation resulted due to the temperature difference between sample and humid air. PbI_2 was formed with no detectable trace of the hydrate crystals. This reaction was not reversible.

We now propose a mechanism to describe how hydration occurs in thin films based on the interpretation of the ellipsometry observations. Ellipsometry spectra were recorded every 10 or 20 min during the conversion of a crystalline MAPI film to $\text{CH}_3\text{NH}_3\text{PbI}_3 \cdot \text{H}_2\text{O}$ by exposure to air with 80% RH over a period of 100 min.

Figure 4a shows a diagram of the conversion model that yielded the most accurate description of the transient ellipsometry data. It describes the hydration process as isotropic and homogeneous, which corresponds mathematically to a

Bruggeman-type mixture of both pristine MAPI and its hydrated counterparts (see the Methods section for details on the Bruggeman approximation). The optical constants of both MAPI and the hydrate phase were determined from a MAPI single crystal and a MAPI single crystal hydrated by exposure to a moist airflow (80% RH) for 60 h (see Figure 1). The three fit parameters in this model are the thickness of the solid thin film, the thickness of the roughness layer on top of the film, and the relative ratio of MAPI and its hydrate in the mixture forming the film and roughness layer. The thickness of the roughness layer was a free parameter during the entire fitting procedure. The thickness of the film and the ratio of its constituents were iteratively defined as fit parameters to avoid the issues arising from the high correlation between these two variables.

Figure 4b shows representative fits to the measured ellipsometry parameters using the isotropic Bruggeman hydration model described in the previous paragraph. In addition to the qualitative agreement, the model is confirmed by a figure of merit, the mean squared error calculated for the simultaneous fit of the nine curves ($\text{MSE} = 5.9$), indicating a close match between modeled and experimental data. An alternative model was also tested that describes the anisotropic

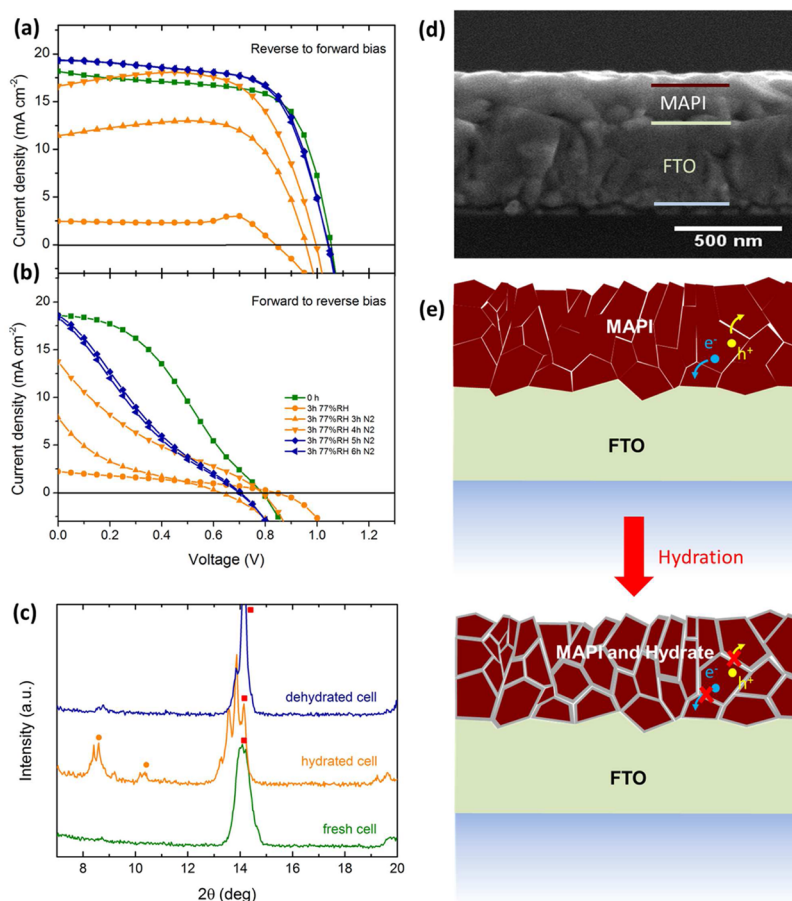


Figure 6. (a, b) Current–voltage (J – V) characteristics showing full recovery of a planar heterojunction MAPI solar cell upon exposure to moisture, scanned from reverse bias to forward bias and from forward bias to reverse bias, respectively. The corresponding performances of the cell are given in Table S4 in the Supporting Information. Note that the steady-state performance of devices prepared in a similar way indicated lower steady-state photocurrents at the maximum power point (see Figure S6 in the Supporting Information). (c) XRD patterns of a device before and after hydration, showing the emergence of the hydrate species. Dots are used to tag the main features, according to the color of their respective spectra. (d) Cross-sectional SEM image of MAPI deposited on a FTO-coated glass slide. (e) Presumed microscopic degradation model of MAPI thin films under partial hydration.

formation of the hydrate as a layer on top of a MAPI film, with progressive conversion of MAPI to hydrate from top to bottom. However, this model could not account for the collected ellipsometry data. Other more sophisticated models such as graded compositions did not significantly improve the fits either. Thus, we conclude that the conversion is isotropic on macroscopic scales (i.e., the average film composition is independent of depth), although the phases are likely to separate on a microscopic scale. This suggests a high degree of penetration of water molecules into MAPI thin films, which might arise from the diffusion of water molecules along the grain boundaries.

Our isotropic model cannot describe the complete degradation process of thin films at exposure times longer than 100 min for two reasons. First, because the optical constants obtained in the single-crystal study are those of the monohydrate. The formation of the dihydrate at longer exposure times modifies the optical constants of the compound, which would require a different, three-component Bruggeman model. Second, a significant increase of the top layer roughness is observed at long exposure times, which causes a dramatic increase of the proportion of scattered light (atomic force micrographs of the film surface for different moisture exposure times are shown in Figure 5, and the change in surface

roughness with time is given in Table S3 in the Supporting Information). Significant roughness (above a value of $\sim\lambda/10$, where λ is the wavelength of the probe beam) must be analyzed with models that are more complex than a single EMA layer with voids. We note that the probe spot of the ellipsometer (~ 1 mm) has a large diameter, compared to the characteristic grain size (~ 50 – 400 nm), which reconciles our homogeneous and isotropic macroscopic conversion model with the microscopic model.

Figure 4c shows the evolution of the modeled hydrate content against moist air exposure time obtained from the ellipsometry fit. It can be correlated with the results from time-resolved X-ray diffraction presented in Figure 3a. Conversely, Figure 4b shows the disappearance of $\text{CH}_3\text{NH}_3\text{PbI}_3\cdot\text{H}_2\text{O}$ upon drying of a hydrated single crystal of MAPI. Conversion of MAPI perovskite to $\text{CH}_3\text{NH}_3\text{PbI}_3\cdot\text{H}_2\text{O}$ causes a lattice expansion of 6%, based on the relative lattice parameters of the two phases (247 \AA^3 per formula unit for MAPI, and 263 \AA^3 for $\text{CH}_3\text{NH}_3\text{PbI}_3\cdot\text{H}_2\text{O}$).^{14,15} Using the fitted hydrate content as a function of exposure time (see Figure 3 in the main text), values of the increase of the solid layer thickness due to its expansion on partial hydration can be estimated. Since the roughness of the top layer is also increased by exposure to moisture, the expansion of the total equivalent thickness is

obtained by adding the increase of the measured top layer roughness to the dilatation of the lattice inferred from the relative ratio of phases. Figure 4d shows that the thickness predicted from the volume fraction and values directly inferred from the ellipsometry fit follow a very similar trend, as would be expected if our model is internally self-consistent. At early exposure times (<60 min), however, the measured total thickness is increasing slowly, compared to the amount of hydrate present in the film. This could indicate that the hydrate is filling voids within the granular films.

The increase in roughness, appearing together with the discoloration of MAPI thin films, because of hydration, is shown in Figure 5, as a function of exposure time. A dramatic increase in roughness is observed at exposure times longer than 90 min, caused by the crystallization of needle-shaped structures on the surface of the films. This corresponds to the appearance of dihydrate XRD reflections in Figure 3a. Therefore, it is likely that these new structures are dihydrate crystals (compare with the photographs of directly synthesized needlelike hydrate crystals in Figure S4 in the Supporting Information). Note that the volume of the dihydrate phase and PbI_2 released upon conversion from $\text{CH}_3\text{NH}_3\text{PbI}_3 \cdot \text{H}_2\text{O}$ is 28% greater than the original volume of MAPI.

State-of-the-Art Solar Cells. Finally, we now extend our investigations to state-of-the-art solar cells to demonstrate the reversibility of the hydration process in functional devices. The solar cells were fabricated according to the protocol detailed in the Methods section. Figure 6a shows the forward-to-reverse bias photocurrent–voltage (J – V) scans measured at different times during exposure of the device to moist air (77% RH) for 3 h, followed by exposure to a dry nitrogen stream for ~5 h. Figure 6b shows the corresponding J – V curves measured with reverse-to-forward bias scans. It is apparent for both scan directions that there is almost an order-of-magnitude drop in the photocurrent and a ~200 mV loss in photovoltage after the device was exposed to moisture for 3 h. Strikingly, following exposure of the device to dry nitrogen for 5 h, the J – V curve recovered to very close to its original state in the case of the forward-to-reverse bias scan. For the reverse-to-forward bias scan, this recovery was much less complete, and we see that the magnitude of the hysteresis³² in the device's J – V curves has increased, following the hydration–dehydration cycle.

Figure 6c demonstrates the concomitant appearance of the characteristic XRD reflections of the monohydrate with the loss in photovoltaic performance seen in Figures 6a and 6b. The XRD measurement was performed on the complete solar cell exposed to moisture and demonstrates the formation of MAPI monohydrate in devices.

The combination of time-resolved XRD and J – V measurements suggests that partial hydration is already sufficient to cause a dramatic drop in PCE. Our ellipsometry modeling implied that the hydration process was isotropic on a macroscopic scale. This observation, combined with the granular nature of the thin film (see Figure 6c), suggests efficient penetration of moisture within the MAPI film along the grain boundaries or micropores/mesopores. These arguments lead us to propose the microscopic degradation mechanism displayed in Figure 6e. Here, the significant loss of PCE after partial conversion to MAPI hydrate may be due to the isolation of the grains from each other, which would rapidly impede charge carrier transport, resulting in increased recombination at the grain interfaces.

It is interesting that the exposure of devices comprising MAPI to moist air at 77% RH and 21 °C did not lead to the irreversible decomposition of MAPI to PbI_2 and HI, as would be the case in the presence of liquid water. In fact, the effect of moisture exposure could be reversed by exposure to a dry gas flow for several hours. However, it is likely that the underlying film underwent microstructural reorganization during this process, which may account for the significantly increased hysteresis observed following the hydration–dehydration cycle.³³

However, this same process can be beneficial during film processing. Since the presence of water vapor appears to catalyze dynamic recrystallization within the film between the hydrated and pure crystalline phases, this may lead to higher-quality films under the optimized processing conditions, as long as water is subsequently completely removed by thermal annealing. We note that the humidity in these studies^{5,6} is lower than ~50%; 60% appears to be the threshold where films are no longer good quality.

CONCLUSIONS

In conclusion, in addition to the precise optical characterization of MAPI and $\text{CH}_3\text{NH}_3\text{PbI}_3 \cdot \text{H}_2\text{O}$, we have shown that the moisture in air induces a reversible hydration process of methylammonium lead iodide perovskite (MAPI). The key difference separating reversible and irreversible degradation seems to be the presence of condensed water. In its absence, no crystalline lead iodide was produced and the reaction can be reversed by blowing dry air over the samples. We demonstrated that the conversion happens isotropically within the granular thin films. The rapid drop of PCE of the devices upon partial hydration led us to propose that the formation of a hydrated layer on the grains has an insulating effect resulting in recombination of photogenerated charge carriers prior to collection.

ASSOCIATED CONTENT

Supporting Information

This material is available free of charge via the Internet at <http://pubs.acs.org/>.

AUTHOR INFORMATION

Corresponding Authors

*E-mail: pablo.docampo@cup.uni-muenchen.de.

*E-mail: piers.barnes@imperial.ac.uk.

Author Contributions

[†]Both authors contributed equally to the work.

Notes

The authors declare no competing financial interest.

ACKNOWLEDGMENTS

P.R.F.B. and A.L. are grateful to the EPSRC (Nos. EP/J002305/1, EP/M014797/1, and EP/M023532/1) for financial support. Y.H., P.D., and T.B. acknowledge funding from the Bavarian Ministry for the Environment, the Bavarian Network “Solar Technologies Go Hybrid”, and the DFG Excellence Cluster Nanosystems Initiative Munich (NIM). We acknowledge support from the European Union through the award of a Marie-Curie Intra-European Fellowship. M.C.-Q. and M.I.A. thank the Spanish Ministry of Economy and Competitiveness for financial support through Project No. MAT2012-37776. O.J.W. would like to thank EPSRC (No. EP/G03768X/1) for a

DTC studentship. A.L. and P.R.F.B. thank Davide Moia for useful discussions.

■ REFERENCES

- (1) Green, M. A.; Emery, K.; Hishikawa, Y.; Warta, W.; Dunlop, E. D. *Prog. Photovoltaics* **2015**, *23*, 1.
- (2) Kojima, A.; Teshima, K.; Shirai, Y.; Miyasaka, T. *J. Am. Chem. Soc.* **2009**, *131*, 6050.
- (3) Snaith, H. J. *J. Phys. Chem. Lett.* **2013**, *4*, 3623.
- (4) Eperon, G. E.; Burlakov, V. M.; Docampo, P.; Goriely, A.; Snaith, H. J. *Adv. Funct. Mater.* **2014**, *24*, 151.
- (5) Bass, K. K.; McAnally, R. E.; Zhou, S.; Djurovich, P. I.; Thompson, M. E.; Melot, B. C. *Chem. Commun.* **2014**, *50*, 15819.
- (6) Zhou, H.; Chen, Q.; Li, G.; Luo, S.; Song, T.-B.; Duan, H.-S.; Hong, Z.; You, J.; Liu, Y.; Yang, Y. *Science* **2014**, *345*, 542.
- (7) Frost, J. M.; Butler, K. T.; Brivio, F.; Hendon, C. H.; van Schilfgaarde, M.; Walsh, A. *Nano Lett.* **2014**, *14*, 2584.
- (8) Niu, G.; Guo, X.; Wang, L. *J. Mater. Chem. A* **2015**, *2*, 705.
- (9) Wakamiya, A.; Endo, M.; Sasamori, T.; Tokitoh, N.; Ogomi, Y.; Hayase, S.; Murata, Y. *Chem. Lett.* **2014**, *43*, 711.
- (10) Noh, J. H.; Im, S. H.; Heo, J. H.; Mandal, T. N.; Seok, S. I. *Nano Lett.* **2013**, *13*, 1764.
- (11) Habisreutinger, S. N.; Leijtens, T.; Eperon, G. E.; Stranks, S. D.; Nicholas, R. J.; Snaith, H. J. *Nano Lett.* **2014**, *14*, 5561.
- (12) Law, C.; Misek, L.; Dimitrov, S.; Shukya-Tuladhar, P.; Li, X.; Barnes, P. R. F.; Durrant, J.; O'Regan, B. C. *Adv. Mater.* **2014**, *26*, 6268.
- (13) Poglitsch, A.; Weber, D. *J. Chem. Phys.* **1987**, *87*, 6373.
- (14) Hao, F.; Stoumpos, C. C.; Liu, Z.; Chang, R. P. H.; Kanatzidis, M. G. *J. Am. Chem. Soc.* **2014**, *136*, 16411.
- (15) Vincent, B. R.; Robertson, K. N.; Cameron, T. S.; Knop, O. *Can. J. Chem.* **1986**, *65*, 1042.
- (16) Christians, J. A.; Herrera, P. A. M.; Kamat, P. V. *J. Am. Chem. Soc.* **2015**, *137*, 1530.
- (17) Yang, J.; Siempelkamp, B. D.; Liu, D.; Kelly, T. L. *ACS Nano* **2015**, *9*, 1955–1963.
- (18) Zhao, Y.; Nardes, A. M.; Zhu, K. *J. Phys. Chem. Lett.* **2014**, *5*, 490.
- (19) Weber, D. *Z. Naturforsch., B: J. Chem. Sci.* **1978**, *33*, 1443.
- (20) Xiao, Z.; Dong, Q.; Bi, C.; Shao, Y.; Yuan, Y.; Huang, J. *Adv. Mater.* **2014**, *26*, 6503.
- (21) Yu, P. Y.; Cardona, M. *Fundamentals of Semiconductors*, 3rd Edition; Springer-Verlag: Berlin, Heidelberg, Germany, 2001.
- (22) Fujiwara, H.; Koh, J.; Rovira, P. I.; Collins, R. W. *Phys. Rev. B* **2000**, *61*, 10832.
- (23) Ball, J. M.; Stranks, S. D.; Horantner, M. T.; Huttner, S.; Zhang, W.; Crossland, E. J. W.; Ramirez, I.; Riede, M.; Johnston, M. B.; Friend, R. H.; Snaith, H. J. *Energy Environ. Sci.* **2015**, *8*, 602.
- (24) Lin, Q.; Armin, A.; Nagiri, R. C. R.; Burn, P.; Meredith, P. *Nat. Photonics* **2015**, *9*, 106.
- (25) Loper, P.; Stuckelberger, M.; Niesen, B.; Werner, J.; Filipic, M.; Moon, S.-J.; Yum, J.-H.; Topic, M.; De Wolf, S.; Ballif, C. *J. Phys. Chem. Lett.* **2015**, *6*, 66.
- (26) Baikie, T.; Fang, Y.; Kadro, J. M.; Schreyer, M.; Wei, F.; Mhaisalkar, S. G.; Graetzel, M.; White, T. J. *J. Mater. Chem. A* **2013**, *1*, 5628.
- (27) Shi, D.; Adinolfi, V.; Comin, R.; Yuan, M.; Alarousu, E.; Buin, A.; Chen, Y.; Hoogland, S.; Rothenberger, A.; Katsiev, K.; Losovyj, Y.; Zhang, X.; Dowben, P. A.; Mohammed, O. F.; Sargent, E. H.; Bakr, O. M. *Science* **2015**, *347*, 519.
- (28) Xie, J.; Liu, Y.; Liu, J.; Lei, L.; Gao, Q.; Li, J.; Yang, S. *J. Power Sources* **2015**, *285*, 349.
- (29) Koustelas, I. B.; Ducasse, L.; Papavassiliou, G. C. *J. Phys.: Condens. Matter* **1996**, *8*, 1217.
- (30) Campoy-Quiles, M.; Nelson, J.; Bradley, D. D. C.; Etchegoin, P. G. *Phys. Rev. B* **2007**, *76*, 235206.
- (31) Hirasawa, M.; Ishihara, T.; Goto, T. *J. Phys. Soc. Jpn.* **1994**, *63*, 3870.
- (32) Snaith, H. J.; Abad, H.; Ball, J. M.; Eperon, G. E.; Leijtens, T.; Noel, N. K.; Stranks, S. D.; Wang, J. T.-W.; Wojciechowski, K.; Zhang, W. *J. Phys. Chem. Lett.* **2014**, *5*, 1511.
- (33) Kim, H.-S.; Park, N. G. *J. Phys. Chem. Lett.* **2014**, *5*, 2927.